

Layer-by-Layer Removal of Insulating Few-Layer Mica Flakes for Asymmetric Ultra-Thin Nanopore Fabrication

Jun Gao¹, Wei Guo¹ (✉), Hua Geng¹, Xu Hou¹, Zhigang Shuai², and Lei Jiang^{1,3} (✉)

¹ Beijing National Laboratory for Molecular Sciences (BNLMS), and Key Laboratory of Organic Solids, Institute of Chemistry, Chinese Academy of Sciences, Beijing 100190, China

² Department of Chemistry, Tsinghua University, Beijing 100084, China

³ School of Chemistry and Environment, Beihang University, Beijing 100191, China

Received: 21 June 2011 / Revised: 27 November 2011 / Accepted: 28 November 2011

© Tsinghua University Press and Springer-Verlag Berlin Heidelberg 2011

ABSTRACT

We demonstrate an elaborate method to controllably fabricate ultra-thin nanopores by layer-by-layer removal of insulating few-layer mica flakes with atomic force microscopy (AFM). The fabricated nanopores are geometrically asymmetric, like an inverted quadrangular frustum pyramid. The nanopore geometry can be engineered by finely tuning the mechanical load on the AFM tip and the scanning area. Particularly noteworthy is that the nanopores can also be fabricated in suspended few-layer mica membranes on a silicon window, and may find potential use as functional components in nanofluidic devices.

KEYWORDS

Two-dimensional materials, mica, few-layer, ultra-thin, solid-state nanopores, atomic force microscopy

1. Introduction

Layered materials, with strong in-plane covalent bonds and weak van der Waals interactions between atomic planes, represent an appealing but largely unexplored source of two-dimensional (2D) materials [1–3]. So far, many bulk materials have been successfully exfoliated into 2D atomic sheets, including graphite, MoS₂, WS₂, MoSe₂, MoTe₂, TaSe₂, NbSe₂, NiTe₂, BN, and Bi₂Sr₂CaCu₂O_x [4].

Among such layered materials, mica is chemically inert and insulating to heat and electricity [5–7]. These attractive chemical and physical properties make mica a favored material for radio frequency capacitors, high voltage electrical insulators, solid lubrication for

nanoscale friction, and atomically flat substrates [8–11]. The crystal structure imparts mica with perfect basal cleavage [12]. Until recently, atomically thin mica sheets have been isolated from bulk materials [13].

The emergence of 2D materials sheds light on the fabrication of ultra-thin solid-state nanopores [14]. In particular, in the applications of nanopore-based analysis and separation [15], ultra-thin nanopores with both length and diameter matching the size of molecular analytes show promising superiorities over previous reported nanopore systems [16–22]. Although the diameter of the state-of-the-art SiN nanopores can be successfully reduced down to 1.5–2 nm, a substantial challenge remains in that none of them has a channel length shorter than 5 nm [23–26]. One disadvantage

Address correspondence to Wei Guo, wguo@iccas.ac.cn; Lei Jiang, jianglei@iccas.ac.cn



of such 5-nm or longer nanochannels, for example in nanopore-based DNA sequencing, is that the recorded ionic current blockades may be induced simultaneously by at least 10 nucleotides in an extended ssDNA chain [27]. To reduce the channel length, biological nanopores with accurate pore size of 1.4 nm and length of 5.2 nm were initially established by self-assembling α -hemolysin proteins into a lipid bilayer [28–30]. The recently reported *Mycobacterium smegmatis* porin A (MspA) nanopores bear a narrow (1.2 nm) aperture and an extremely short (0.5 nm) channel [31, 32]. Although these biological nanopores have more precisely controlled structure, they rely on the lipid membrane, which is mechanically fragile, electrically noisy, and incompatible with other nanodevice components [33–36]. In addition, the genetic engineering methods for tailoring the composition of the protein pores are not straightforward [37], especially for researchers in the field of physical and chemical sciences [38, 39].

To tackle these challenges, ultra-thin nanopores constructed in graphene membranes have attracted much interest due to their extraordinary properties [40–43]. For example, in graphene nanopore devices, the in-plane conductivity is sensitive to the immediate surface environment, which can be used as an indicator of the target analyte. However, to date, besides highly conducting graphene, ultra-thin nanopores fabricated in insulating 2D materials have not been reported in the literature.

Herein, we demonstrate an elaborate method to controllably fabricate ultra-thin solid-state nanopores in few-layer mica flakes with single layer resolution (ca. 1.0 nm). Through an atomic force microscopic (AFM) micromechanical fabrication process, individual mica layers can be removed one-by-one from the few-layer mica substrate and finally form a penetrated nanopore within the scanning area. The fabricated nanopores are geometrically asymmetric, like an inverted quadrangular frustum pyramid (Fig. 1). The nanopore geometry can be engineered by finely tuning the mechanical load and the scanning area. Particularly noteworthy is that this AFM micromechanical processing method can be equally applied to a suspended ultra-thin mica membrane on a silicon window to fabricate nanopores. In principle, this method can

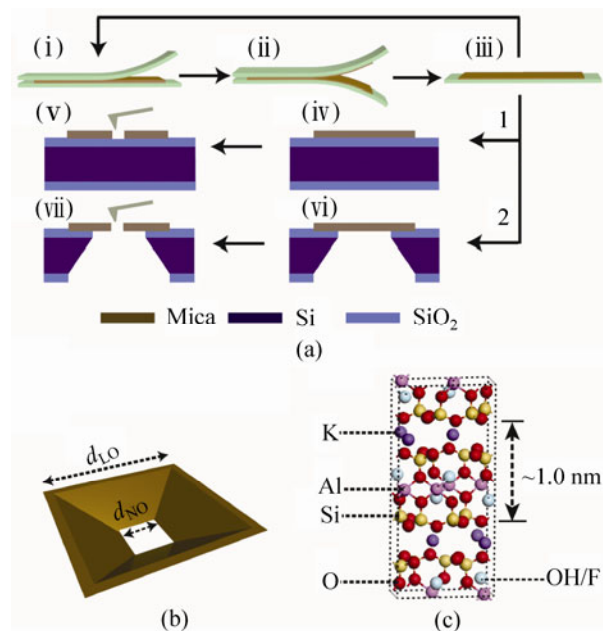


Figure 1 Schematic illustration of few-layer mica cleavage and nanopore fabrication. (a) A freshly cleaved bulk muscovite mica sheet is attached to a sticky tape. Few-layer mica is prepared by repeatedly peeling off small flakes with other fresh pieces of tape (i)–(iii). The peeled flakes can be transferred onto the top of either a solid silicon substrate (route 1) or a silicon window (route 2) for further characterization and processing. Nanopores can be fabricated in both solid (iv) and (v) and suspended (vi) and (vii) few-layer mica membranes by AFM processing with a certain mechanical load. (b) The nanopores are geometrically asymmetric, like an inverted quadrangular frustum pyramid. The widths of the large and small openings are denoted as d_{LO} and d_{NO} , respectively. (c) Crystal structure of mica. The thickness of a mica monolayer is ca. 1.0 nm

also be expected to pattern non-specific 2D substrates with the desired number of atomic layers for planar nanoelectronic devices [44].

2. Experimental

2.1 Fabrication and characterization of few-layer mica membranes

A freshly cleaved muscovite mica (Alfa Aesar) sheet was attached to a sticky tape (Scotch 600, 3M). The few-layer mica flakes were prepared by repeatedly peeling off small flakes with other pieces of fresh sticky tape at least four times. Silicon wafers with a capping oxidized layer of 0 nm, 250 nm, 300 nm, or 500 nm thick were used as substrate for optical characterization. After transfer onto the Si/SiO₂ substrate, the few-layer

mica flakes were characterized with optical microscopy (Olympus BX51 microscope with a Nikon DS-Ri1 camera) and followed by AFM measurements (Seiko SPI3800N) to determine the actual thickness. In optical characterization, the red green blue (RGB) values of five neighboring pixels were averaged. The mechanical load for AFM imaging is about 80 nN [45].

Two-terminal I - V measurements on the few-layer mica flakes were conducted using a Keithley 4200-SCS semiconductor system and Suss PM5 analytical probe station in a clean and shielded cage under dark conditions. Two platinum probes were employed in the I - V measurements. The distance between two electrodes was about 20 μm and 50 μm , respectively, for the measurements on mica flakes and SiO_2 substrate.

2.2 Calculation methods

Optimized geometries and band structures of bulk and single-layer mica were computed using density functional theory (DFT) in the generalized gradient approximation (GGA) with the Perdew–Burke–Ernzerhof (PBE) exchange correlation function as implemented in the CASTEP program [46]. The total energy and the force convergence thresholds were 2×10^{-5} eV/atom and $0.05 \text{ eV} \cdot \text{\AA}^{-1}$, respectively. A plane wave cut-off was chosen as 300 eV for the ultra-soft pseudopotential [47]. Integrations over the Brillouin zone were carried out by using the Monkhorst–Pack scheme with $4 \times 4 \times 1$ k -sampling in the relevant irreducible wedge [48]. Since DFT always underestimate the band gap [49], the band shift was calibrated using experimental data [50].

2.3 Micromechanical fabrication of nanopores on few-layer mica membranes

The AFM was operated in contact mode. The AFM tip (NSC11, Mikromasch) was made of silicon with a silicon nitride coating. The tip radius was about 20 nm and the full tip angle was ca. 40° (Fig. S-5 in the Electronic Supplementary Material (ESM)). All processing was carried out at a scanning rate of 1 Hz. Different loads, from 800–4000 nN, and different scanning areas, from $15 \text{ nm} \times 15 \text{ nm}$ to $500 \text{ nm} \times 500 \text{ nm}$, were employed to scan the few-layer mica surface. After

each mechanical processing, an adjacent area of $\sim 2 \mu\text{m}$ was imaged *in situ* with a much lower mechanical load of 80 nN. Before each experiment, the machine was thermally equilibrated for at least 4 h.

We also prepared Si/ SiO_2 bilayer structures with a penetrated single window in the center to support the ultra-thin mica membranes. A series of microfabrication processes were employed to fabricate the silicon window. Experimental details can be found in the ESM. Ultra-thin mica flakes were transferred onto the silicon window by a mechanical cleavage method. Some individual mica flakes were eventually found to cover the silicon window. By using a similar AFM fabrication method, nanopores can be drilled in the suspended mica membranes. The mechanical load on the AFM tip was 3000 to 7500 nN.

3. Results and discussion

Considering the crystal structure of mica, each two sheets of aluminum (or magnesium) stabilized silica tetrahedra (SiO_4) are interconnected by potassium ions via weak van der Waals interactions [12]. We define such an atomic complex of thickness ca. 1.0 nm as one mica monolayer (Fig. 1(c)). As schematically illustrated in Fig. 1(a), few-layer mica flakes ($n < 10$, where n is the number of mica monolayers) were prepared by repeatedly peeling off small flakes with pieces of sticky tape [1]. The peeled flakes were first transferred to the top of an oxidized silicon wafer before preliminary identification by optical microscopy. These 2D crystallites atop the Si/ SiO_2 wafer become visible due to the changes in interference color with respect to the blank substrate (phase contrast) [51, 52]. The visual inspection provides a convenient way to determine the relative position of these ultra-thin crystals on the silicon wafer. Further analysis of the actual thickness of the peeled flakes was performed by AFM. On a given substrate, once the relationship between the optical contrast and the actual membrane thickness has been determined, a precise and concise identification of few-layer mica flakes can be realized using only optical observation. For comparison, silicon wafers with different capping oxide layers of 0 nm, 250 nm, 300 nm or 500 nm thickness were used as substrates for optical and AFM characterization.



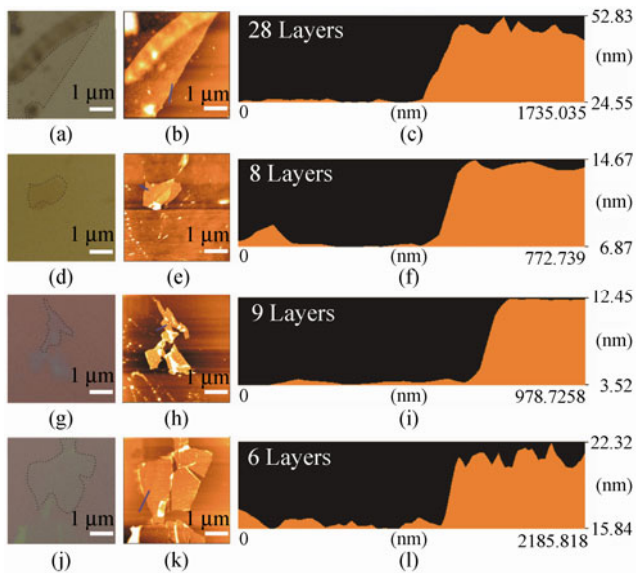


Figure 2 Optical and AFM characterization of the few-layer mica flakes. Typical results for silicon wafers with different capping oxide layers of 0 nm (a)–(c), 250 nm (d) and (f), 300 nm (g)–(i) and 500 nm (j)–(l) thicknesses are shown. We focus on the thinnest visible mica layer on the Si/SiO₂ substrate with a transparent border that is nearly indistinguishable from the blank substrate (highlighted by the dashed line). The two methods indicate identical morphologies of the mica sheets. AFM observation reveals the actual height of the thinnest mica layer that can be observed under optical microscopy (c, f, i, l)

The RGB values of each pixel measured with a charge-coupled device (CCD) camera were converted to grayscale values according to the following equation [53]:

$$I_{\text{grey}} = 0.30 I_{\text{red}} + 0.59 I_{\text{green}} + 0.11 I_{\text{blue}} \quad (1)$$

where I_x stands for the optical intensity in x channel (x = gray, red, green or blue). Then the optical contrast (OC) between the mica sheet (mica) and the silicon substrate (sub) can be calculated as [54]:

$$\text{OC} = \frac{|I_{\text{gray,sub}} - I_{\text{gray,mica}}|}{I_{\text{gray,sub}} + I_{\text{gray,mica}}} \quad (2)$$

Previous studies have pointed out that thinner sheets exhibit minor optical contrast [55]. To find the thinnest visible mica layers on the Si/SiO₂ substrate, we focused on those mica flakes with a transparent border that nearly indistinguishable from the blank substrate. Figure 2 shows the thinnest visible mica flakes in optical imaging. Their actual height was measured with AFM. The two methods indicate identical morphology

of the same mica flakes. The optical contrasts for the thinnest mica flakes on all four kinds of substrate are within $2.0 \pm 0.3\%$, which is very near the resolution limit of the naked human eye (1.5%) [56].

The experimental results show that the presence of an oxidized layer atop the silicon wafer is of great importance in obtaining thinner mica flakes. With a bare silicon substrate, the thinnest visible mica layer contained approximately 28 mica monolayers. With an increase in the thickness of the capping SiO₂ layer up to 500 nm, the thinnest visible mica layer was significantly reduced to merely 6 monolayers. This result is qualitatively in agreement with previous studies in which a thin layer of SiO₂ on silicon wafer enhanced the visibility of some 2D materials [57]. The mechanical cleavage approach combined with the optical and AFM characterization was found to be high-yield and reliable, producing ultra-thin mica flakes with typical lateral size of $\sim 10 \mu\text{m}$ and membrane thickness less than 10 nm.

In addition, we tested the electrical insulating properties of the isolated 2D mica sheets. Figure 3(a) schematically illustrates the two-terminal I – V measurement of the few-layer mica on a Si/SiO₂ substrate (see the Experimental section). Almost symmetric I – V curves were obtained for measurements on both the silicon substrate and n mica flakes (Fig. 3(b)). The specific conductivity (σ) can be extracted from the I – V data. For example, the specific conductivity measured for a ten-layer mica flake was about $2.3 \times 10^{-7} \text{ S/m}$, which is higher than that measured for the 500 nm-thick SiO₂ substrate ($0.5 \times 10^{-8} \text{ S/m}$). Based on the electrical conductivity measurements, we can further estimate the breakdown electric field (the breakdown strength, BDS) of the few-layer mica (see the ESM). The BDS of a ten-layer mica sheet was $\sim 59.9 \text{ MV/m}$, which is about one half of the bulk value ($\sim 118 \text{ MV/m}$). However, it is still very large compared to other insulating materials, such as SiO₂ (BDS $\sim 2.6 \text{ MV/m}$). Therefore, few-layer mica preserves excellent insulating properties, even if it is lower than the bulk material.

This experimental result can be verified by first-principles calculation of the electronic band structure of bulk and single-layer mica. As shown in Fig. 3(c), although the band gap for a single-layer mica ($\sim 5.7 \text{ eV}$) is lower than the bulk material ($\sim 7.8 \text{ eV}$), it still

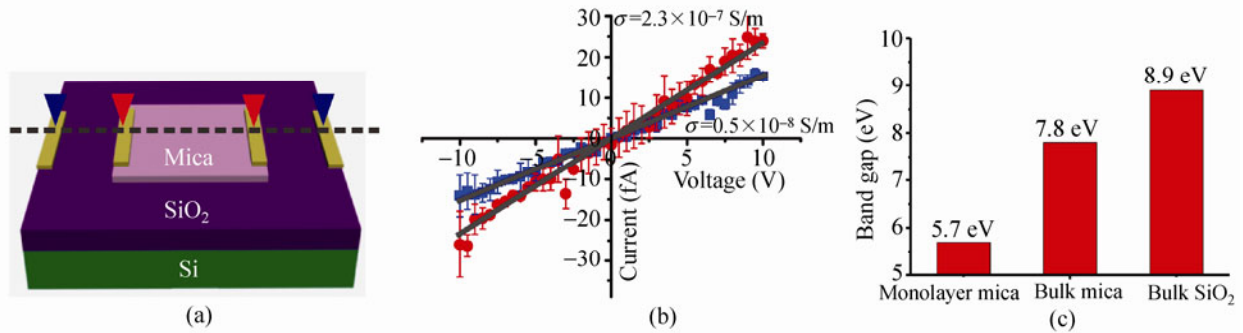


Figure 3 Conductance measurements on few-layer mica flakes. (a) Illustration of the two-terminal I - V measurements of the few-layer mica on a Si/SiO₂ substrate. (b) Representative I - V curves obtained on the 10-layer mica flakes (red) and on the Si/SiO₂ substrate (blue). (c) First-principles calculation of the band gap of a mica monolayer, bulk mica and bulk SiO₂

belongs to the class of insulating materials (taking the band gap of bulk SiO₂ as a reference). A reduction in band gap after being exfoliated into atomically thin sheets has also been found for other 2D materials, such as hexagonal boron nitride (*h*-BN) [58]. A detailed discussion of the variation in band structure is beyond the scope of this work.

In the AFM imaging process, the mechanical load on the AFM tip is very small, and thus no physical damage can be found in the scanning area. When the load exceeds a threshold value (~130 nN for bulk mica) [45], the pressing force causes physical damage

to the mica substrate (see the ESM). By finely tuning the mechanical load on the AFM tip, the 2D mica substrate can be removed layer-by-layer.

To demonstrate this idea, a piece of few-layer mica flake ($n = 9$) was optically selected from the peeled flakes and its actual thickness was determined by AFM. Typical results are shown in Fig. 4. The scanning area was 120 nm × 120 nm. The drilled depth increases with the magnitude of the mechanical load. The minimum step increment was found to be about 1 nm, which is exactly the thickness of a single mica monolayer. The drilled depth can be well-controlled

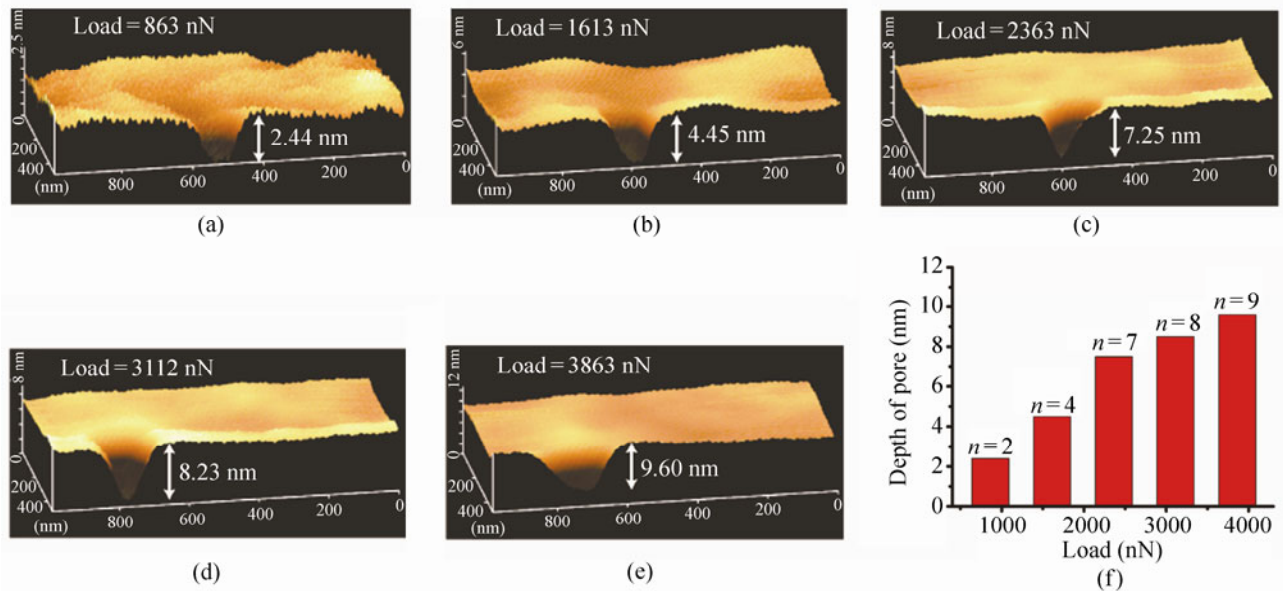


Figure 4 Layer-by-layer removal of few-layer mica with AFM microfabrication method. (a)–(e) AFM images showing the processing area of 120 nm × 120 nm with different mechanical loads on the AFM tip. The few-layer mica substrate contains nine mica monolayers in all. (f) The drilled depth increased with the magnitude of the load. The minimum step increment is ca. 1.0 nm, which is exactly the thickness of a single mica monolayer. By finely tuning the mechanical load, the removed thickness can be engineered from two to nine mica monolayers

from two to nine monolayers (until the mica substrate is penetrated). This AFM micromechanical fabrication method can be employed to fabricate nanostructures on a few-layer mica surface. It can be generally extended to pattern non-specific 2D materials at a desired location and with a controllable number of layers.

As a fundamental application of this AFM micromechanical processing method, a penetrated ultra-thin nanopore was fabricated on a 9.50 nm thick mica substrate (Fig. 5 and Fig. S-2 (in the ESM)). The scanning area was $250\text{ nm} \times 250\text{ nm}$ and the load on AFM tip was 3863 nN. The drilled nanopore exhibits asymmetric geometry, shrinking from the top mica surface to the bottom silicon substrate. The width of the large opening (d_{LO}) was ca. 220 nm, which is approximately identical to the scanning length. The width of the narrow opening (d_{NO}) in contact with the silicon substrate was merely 68 nm. The measured depth of the nanopore was about 9.63 nm, in general agreement with the height of the mica substrate. Optical evidence further proves that the few-layer mica substrate was penetrated. The mean optical contrast between the processing area and the surrounding mica surface is $\sim 2.5\%$, which is approximately the difference between the mica surface and the blank SiO_2 substrate. The optical contrast between the center

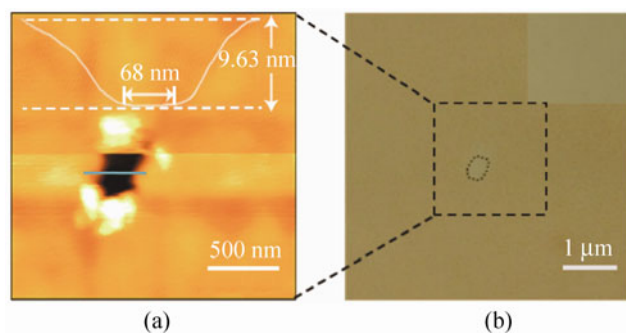


Figure 5 Optical and AFM characterization of the fabricated nanopore. (a) AFM image of an asymmetric ultra-thin nanopore processed with $250\text{ nm} \times 250\text{ nm}$ scanning area on a 9.50 nm mica layer. The insert height image shows the profile of the nanopore, which is geometrically asymmetric. The load on the AFM tip was 3863 nN. (b) The same area viewed by optical microscopy. The dashed line highlights the optical contrast (OC) between the hollow nanopore region and the surrounding mica surface (OC $\sim 2.5\%$). The insert figure shows the optical image of the surrounding silicon substrate whose OC with respect to the nanopore center is merely 0.02%. These results prove that the nanopore is penetrated

of the processing area and the blank silicon substrate is merely 0.02%, indicating that the center of the nanopore and the SiO_2 substrate are at the same height (Fig. 5(b)).

The size of the nanopore can be controlled by tuning the scanning area, as shown in Fig. 6. When the scanning area was larger than $100\text{ nm} \times 100\text{ nm}$, the width of the large opening (d_{LO}) generally agreed with the scanning length (Fig. 6(c)). However, when the scanning length was reduced to below 100 nm, the width of the large opening significantly diverged from the scanning length and became less predictable (see also Fig. S-4 in the ESM). Therefore, further discussion concerning control over the size of the narrow opening is focused on the scanning area larger than $100\text{ nm} \times 100\text{ nm}$. The width of the narrow opening (d_{NO}) is about one tenth to a half of the scanning length. It generally increases with the scanning length, but at a speed much slower than the large opening (Figs. 6(c) and 6(d)). Statistical results on more than sixty nanopores show that the minimum width of the narrow opening is about 20 nm (Figs. 6(a) and 6(d)). We envision that the limitation is caused by the size of the AFM tip, which is also ca. 20 nm at its narrowest end (Fig. S-5 in the ESM). Further studies concerning the structural damage to the ultra-thin mica flakes are of essential importance in understanding the shaping mechanism of the asymmetric nanopores.

An inverted three-dimensional image of the asymmetric nanopore can be visualized as shown in Fig. 6(b). It is interesting to note that the drilled nanopore exhibit an asymmetric geometry, like an inverted quadrangular frustum pyramid. In nanofluidic systems, the asymmetric geometry functions not only as a pathway for molecular transportation, but also provides a geometric kinetic constraint that possibly induces a unidirectional diffusive flow through the nanopore [59, 60]. Studies on the application of geometry-induced asymmetric diffusion for bio-inspired energy conversion and oil/water separation are currently underway in our lab [61–64].

Based on the above discussion, the nanopore fabrication can be further optimized. By employing a smaller AFM tip (maybe a few to ten nanometers), the width of the narrow opening (d_{NO}) should be further reduced. In addition, although a large AFM

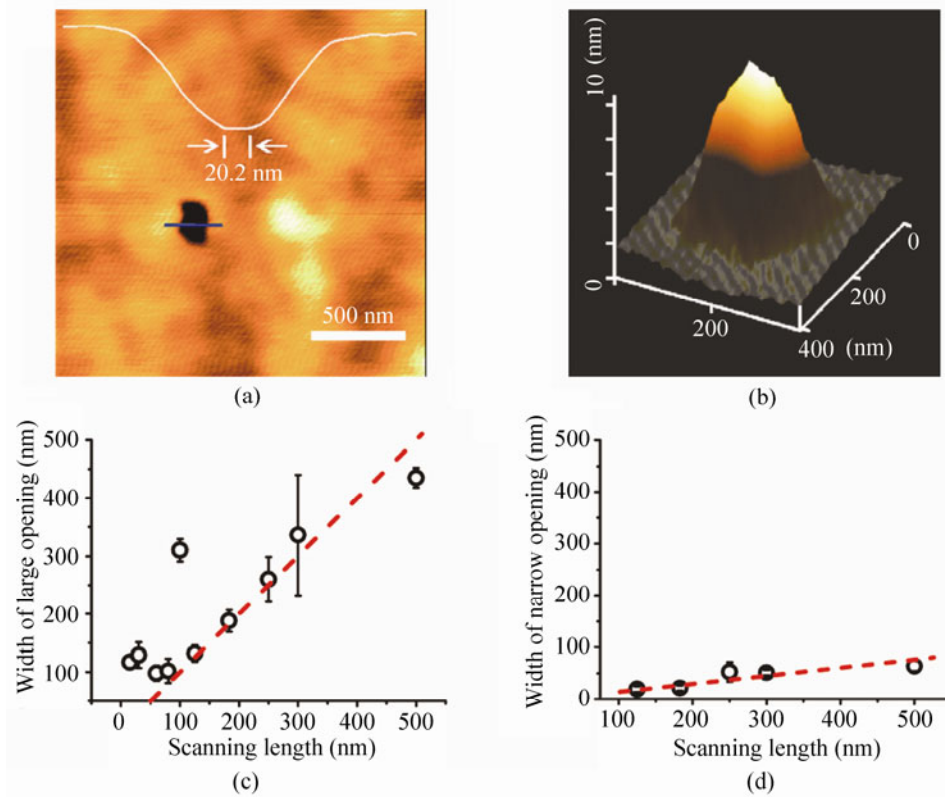


Figure 6 Controlling the nanopore size by tuning the scanning length. (a) AFM image of a nanopore fabricated for a scanning area of 125 nm × 125 nm on an 8-nm-thick mica flake. The large and narrow openings are approximately 160 nm and 20 nm respectively. (b) Inverted three-dimensional image of the asymmetric nanopore identifies an inverted quadrangular frustum pyramid shape. (c) The width of the large opening generally agrees with the scanning length in the range 100–500 nm. Below this region, the micromechanical fabrication process becomes less controllable. (d) The width of the narrow opening generally increases with increasing scanning length, but at a much slower rate than the large opening

scanning area makes the fabrication more controllable, it enlarges the width of the narrowest end. Balancing the controllability and the desired small dimension of one end, a scanning length of 100–120 nm is preferred.

More importantly, using a similar method, nanopores can be also fabricated in suspended ultra-thin mica membranes. A silicon window with a large opening of 560 μm and a small opening of 18 μm was opened in a 400-μm-thick Si/SiO₂ bilayer structure (Fig. 7(a) and Fig. S-7 (in the ESM)) [65]. Few-layer mica membranes were prepared by mechanical cleavage and then transferred onto the silicon window. Individual mica flakes were eventually found to cover the silicon window, as shown in Figs. 7(b)–7(d). Through the AFM processing, a single nanopore of 4.94 nm in depth, and 130 nm at the wide end, and 21.3 nm at the narrow end was fabricated within the scanning area

(Fig. 7(d)). The mechanical load on the AFM tip was 5476 nN in the fabrication process. To obtain penetrated nanopores in the suspended mica membrane, the applied force required was about three times the value used for the solid substrate. One possible reason for this is the elastic property of the suspended mica sheet [66]. The suspended few-layer mica membranes containing a single nanopore may be further developed to give functional nanofluidic devices for molecular sensing [15].

4. Conclusions

We have demonstrated an AFM micromechanical processing method to controllably fabricate asymmetric ultra-thin nanopores in both solid and suspended insulating few-layer mica membranes. The width of the

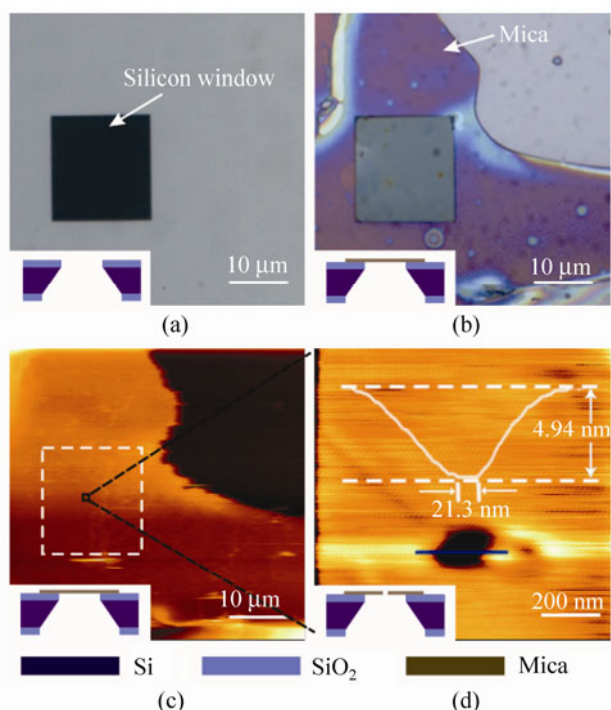


Figure 7 Fabrication of a single nanopore on a suspended ultra-thin mica membrane. (a) A silicon window (in the dark region) was opened on a 400- μm -thick Si/SiO₂ substrate. Both optical (b) and AFM images (c) show that the silicon window was covered by individual mica nanoflakes. The dashed region in (c) shows the underlying silicon window. (d) A magnified view of the nanopore region. The height profile of the cross section shows the nanopore is about 4.94 nm in depth, 130 nm at the wide end, and 21.3 nm at the narrow end

large opening generally agrees with the scanning length and the small opening is restricted to the size of the AFM tip. The nanopore geometry can be engineered by finely tuning the mechanical load and the scanning area. The AFM micromechanical fabrication can be generally employed to pattern non-specific 2D substrates with single atomic layer resolution. The geometrically asymmetric ultra-thin nanopores in suspended few-layer mica membranes may have potential uses in constructing functional nanofluidic devices.

Acknowledgements

We thank Dr. Bin Su and Mr. Changqing Ye in Institute of Chemistry, Chinese Academy of Sciences (ICCAS) for technical help and Prof. Fan Xia in Huazhong University of Science and Technology

(HUST) for beneficial discussion. This work was financially supported by the National Research Fund for Fundamental Key Projects (Nos. 2011CB935700, 2010CB934700, and 2009CB930404) and the National Natural Science Foundation of China (Nos. 90923004, 91127025, 20920102036, 20974113, 21121001, 21103201, and 21071148). The Chinese Academy of Sciences is gratefully acknowledged.

Electronic Supplementary Material: Supplementary material (AFM characterization of the few-layer mica nanosheets for nanopore fabrication, the differences between AFM imaging and AFM micromechanical fabrication, nanopore morphology with different processing areas, scanning electron microscope (SEM) characterization of the AFM tips, and estimation of the breakdown strength, fabrication of ultra-thin nanopore on suspended few-layer mica membranes.) is available in the online version of this article at <http://dx.doi.org/10.1007/s12274-011-0189-7> and is accessed free of charge.

References

- [1] Novoselov, K. S.; Jiang, D.; Schedin, F.; Booth, T. J.; Khotkevich, V. V.; Morozov, S. V.; Geim, A. K. Two-dimensional atomic crystals. *Proc. Natl. Acad. Sci. USA* **2005**, *102*, 10451–10453.
- [2] Hernandez, Y.; Nicolosi, V.; Lotya, M.; Blighe, F. M.; Sun, Z. Y.; De, S.; McGovern, I. T.; Holland, B.; Byrne, M.; Gun'ko Y. K. et al. High-yield production of graphene by liquid-phase exfoliation of graphite. *Nat. Nanotechnol.* **2008**, *3*, 563–568.
- [3] Koh, Y. K.; Bae, M. H.; Cahill, D. G.; Pop, E. Reliably counting atomic planes of few-layer graphene ($n > 4$). *ACS Nano* **2011**, *5*, 269–274.
- [4] Coleman, J. N.; Lotya, M.; O'Neill, A.; Bergin, S. D.; King, P. J.; Khan, U.; Young, K.; Gaucher, A.; De, S.; Smith, R. J. et al. Two-dimensional nanosheets produced by liquid exfoliation of layered materials. *Science* **2011**, *331*, 568–571.
- [5] Caseri, W. R.; Shelden, R. A.; Suter, U. W. Preparation of muscovite with ultrahigh specific surface-area by chemical cleavage. *Colloid Polym. Sci.* **1992**, *270*, 392–398.
- [6] Maslova, M. V.; Gerasimova, L. G.; Forsling, W. Surface properties of cleaved mica. *Colloid J.* **2004**, *66*, 322–328.
- [7] Jin, P.; Mukaibo, H.; Horne, L. P.; Bishop, G. W.; Martin, C. R. Electroosmotic flow rectification in pyramidal-pore mica membranes. *J. Am. Chem. Soc.* **2010**, *132*, 2118–2119.

- [8] Augustin, L.; Chi, L. F.; Fuchs, H.; Hoppner, S.; Rakers, S.; Rothig, C.; Schwaack, T.; Starrberg, F. Preparation and characterization of low-dimensional nanostructures. *Appl. Surf. Sci.* **1999**, *141*, 219–227.
- [9] Lui, C. H.; Liu, L.; Mak, K. F.; Flynn, G. W.; Heinz, T. F. Ultraflat graphene. *Nature* **2009**, *462*, 339–341.
- [10] Singh, M.; Kaur, N.; Singh, L. Morphology of heavy ions irradiated mica. *Radiat. Phys. Chem.* **2010**, *79*, 1180–1188.
- [11] Xu, K.; Cao, P. G.; Heath, J. R. Graphene visualizes the first water adlayers on mica at ambient conditions. *Science* **2010**, *329*, 1188–1191.
- [12] Downs, R. T.; Hall-Wallace, M. The American Mineralogist Crystal Structure Database. *Am Mineral.* **2003**, *88*, 247–250.
- [13] Castellanos-Gomez, A.; Wojtaszek, M.; Tombros, N.; Agraft, N.; van Wees, B. J.; Rubio-Bollinger, G. Atomically thin mica flakes and their application as ultrathin insulating substrates for graphene. *Small* **2011**, *7*, 2491–2497.
- [14] Garaj, S.; Hubbard, W.; Reina, A.; Kong, J.; Branton, D.; Golovchenko, J. A. Graphene as a subnanometre trans-electrode membrane. *Nature* **2010**, *467*, 190–193.
- [15] Branton, D.; Deamer, D. W.; Marziali, A.; Bayley, H.; Benner, S. A.; Butler, T.; Di Ventra, M.; Garaj, S.; Hibbs, A.; Huang, X. H. et al. The potential and challenges of nanopore sequencing. *Nat. Biotechnol.* **2008**, *26*, 1146–1153.
- [16] Schneider, G. F.; Kowalczyk, S. W.; Calado, V. E.; Pandraud, G.; Zandbergen, H. W.; Vandersypen, L. M. K.; Dekker, C. DNA translocation through graphene nanopores. *Nano Lett.* **2010**, *10*, 3163–3167.
- [17] Merchant, C. A.; Healy, K.; Wanunu, M.; Ray, V.; Peterman, N.; Bartel, J.; Fischbein, M. D.; Venta, K.; Luo, Z. T.; Johnson, A. T. et al. DNA translocation through graphene nanopores. *Nano Lett.* **2010**, *10*, 2915–2921.
- [18] Howorka, S.; Siwy, Z. Nanopore analytics: Sensing of single molecules. *Chem. Soc. Rev.* **2009**, *38*, 2360–2384.
- [19] Mulero, R.; Prabhu, A. S.; Freedman, K. J.; Kim, M. J. Nanopore-based devices for bioanalytical applications. *JALA* **2010**, *15*, 243–252.
- [20] Vlassiouk, I.; Apel, P. Y.; Dmitriev, S. N.; Healy, K.; Siwy, Z. S. Versatile ultrathin nanoporous silicon nitride membranes. *Proc. Natl. Acad. Sci. USA* **2009**, *106*, 21039–21044.
- [21] Wanunu, M.; Dadosh, T.; Ray, V.; Jin, J. M.; McReynolds, L.; Drndic, M. Rapid electronic detection of probe-specific microRNAs using thin nanopore sensors. *Nat. Nanotechnol.* **2010**, *5*, 807–814.
- [22] Deamer, D. W.; Branton, D. Characterization of nucleic acids by nanopore analysis. *Accounts. Chem. Res.* **2002**, *35*, 817–825.
- [23] Li, J.; Stein, D.; McMullan, C.; Branton, D.; Aziz, M. J.; Golovchenko, J. A. Ion-beam sculpting at nanometre length scales. *Nature* **2001**, *412*, 166–169.
- [24] Dekker, C. Solid-state nanopores. *Nat. Nanotechnol.* **2007**, *2*, 209–215.
- [25] Striemer, C. C.; Gaborski, T. R.; McGrath, J. L.; Fauchet, P. M. Charge- and size-based separation of macromolecules using ultrathin silicon membranes. *Nature* **2007**, *445*, 749–753.
- [26] Storm, A. J.; Chen, J. H.; Ling, X. S.; Zandbergen, H. W.; Dekker, C. Fabrication of solid-state nanopores with single-nanometre precision. *Nat. Mater.* **2003**, *2*, 537–540.
- [27] Zwolak, M.; Di Ventra, M. Colloquium: Physical approaches to DNA sequencing and detection. *Rev. Mod. Phys.* **2008**, *80*, 141–165.
- [28] Bayley, H.; Cremer, P. S. Stochastic sensors inspired by biology. *Nature* **2001**, *413*, 226–230.
- [29] Stoddart, D.; Maglia, G.; Mikhailova, E.; Heron, A. J.; Bayley, H. Multiple base-recognition sites in a biological nanopore: Two heads are better than one. *Angew. Chem. Int. Edit.* **2010**, *49*, 556–559.
- [30] Stoddart, D.; Heron, A. J.; Mikhailova, E.; Maglia, G.; Bayley, H. Single-nucleotide discrimination in immobilized DNA oligonucleotides with a biological nanopore. *Proc. Natl. Acad. Sci. USA* **2009**, *106*, 7702–7707.
- [31] Butler, T. Z.; Pavlenok, M.; Derrington, I. M.; Niederweis, M.; Gundlach, J. H. Single-molecule DNA detection with an engineered MSPA protein nanopore. *Proc. Natl. Acad. Sci. USA* **2008**, *105*, 20647–20652.
- [32] Derrington, I. M.; Butler, T. Z.; Collins, M. D.; Manrao, E.; Pavlenok, M.; Niederweis, M.; Gundlach, J. H. Nanopore DNA sequencing with MSPA. *Proc. Natl. Acad. Sci. USA* **2010**, *107*, 16060–16065.
- [33] Siwy, Z. S.; Howorka, S. Engineered voltage-responsive nanopores. *Chem. Soc. Rev.* **2010**, *39*, 1115–1132.
- [34] Bocquet, L.; Charlaix, E. Nanofluidics, from bulk to interfaces. *Chem. Soc. Rev.* **2010**, *39*, 1073–1095.
- [35] Xia, F.; Guo, W.; Mao, Y. D.; Hou, X.; Xue, J. M.; Xia, H. W.; Wang, L.; Song, Y. L.; Ji, H.; Ouyang, Q. et al. Gating of single synthetic nanopores by proton-driven DNA molecular motors. *J. Am. Chem. Soc.* **2008**, *130*, 8345–8350.
- [36] Hou, X.; Guo, W.; Jiang, L. Biomimetic smart nanopores and nanochannels. *Chem. Soc. Rev.* **2011**, *40*, 2385–2401.
- [37] Nelson, D. L.; Cox, M. M. *Lehninger Principles of Biochemistry—Fourth Edition*. W. H. Freeman: New York, 2005; pp. 306–330.
- [38] Gyurcsanyi, R. E. Chemically-modified nanopores for sensing. *Trends Anal. Chem.* **2008**, *27*, 627–639.
- [39] Mendes, P. M. Stimuli-responsive surfaces for bio-applications. *Chem. Soc. Rev.* **2008**, *37*, 2512–2529.
- [40] Min, S. K.; Kim, W. Y.; Cho, Y.; Kim, K. S. Fast DNA sequencing with a graphene-based nanochannel device. *Nat. Nanotechnol.* **2011**, *6*, 162–165.



- [41] Huang, S.; He, J.; Chang, S.; Zhang, P.; Liang, F.; Li, S.; Tuchband, M.; Fuhrmann, A.; Ros, R.; Lindsay, S. Identifying single bases in a DNA oligomer with electron tunnelling. *Nat. Nanotechnol.* **2010**, *5*, 868–873.
- [42] Postma, H. W. C. Rapid sequencing of individual DNA molecules in graphene nanogaps. *Nano Lett.* **2010**, *10*, 420–425.
- [43] Prasongkit, J.; Grigoriev, A.; Pathak, B.; Ahuja, R.; Scheicher, R. H. Transverse conductance of DNA nucleotides in a graphene nanogap from first principles. *Nano Lett.* **2011**, *11*, 1941–1945.
- [44] Dimiev, A.; Kosynkin, D. V.; Sinitskii, A.; Slesarev, A.; Sun, Z.; Tour, J. M. Layer-by-layer removal of graphene for device patterning. *Science* **2011**, *331*, 1168–1172.
- [45] Miyake, S. 1 nm deep mechanical processing of muscovite mica by atomic force microscopy. *Appl. Phys. Lett.* **1995**, *67*, 2925–2927.
- [46] Umabayashi, T.; Yamaki, T.; Itoh, H.; Asai, K.. Band gap narrowing of titanium dioxide by sulfur doping. *Appl. Phys. Lett.* **2002**, *81*, 454–456.
- [47] Weng, H.; Yang, X.; Dong, J.; Mizuseki, H.; Kawasaki, M.; Kawazoe, Y. Electronic structure and optical properties of the Co-doped anatase TiO₂ studied from first principles. *Phys. Rev. B* **2004**, *69*, 125219.
- [48] Monkhorst, H. J.; Pack, J. D. Special points for Brillouin-zone integrations. *Phys. Rev. B* **1976**, *13*, 5188–5192.
- [49] Sham, L. J.; Schlüter, M. Density-functional theory of the band gap. *Phys. Rev. B* **1985**, *32*, 3883–3889.
- [50] Davidson, A. T.; Vickers, A. F. The optical properties of mica in the vacuum ultraviolet. *J. Phys. C: Solid State Phys.* **1972**, *5*, 879–887.
- [51] Jung, I.; Pelton, M.; Piner, R.; Dikin, D. A.; Stankovich, S.; Watcharotone, S.; Hausner, M.; Ruoff, R. S. Simple approach for high-contrast optical imaging and characterization of graphene-based sheets. *Nano Lett.* **2007**, *7*, 3569–3575.
- [52] Gaskell, P. E.; Skulason, H. S.; Rodenchuk, C.; Szkopek, T. Counting graphene layers on glass via optical reflection microscopy. *Appl. Phys. Lett.* **2009**, *94*, 143101.
- [53] Nolen, C. M.; Denina, G.; Teweldebrhan, D.; Bhanu, B.; Balandin, A. A. High-throughput large-area automated identification and quality control of graphene and few-layer graphene films. *ACS Nano* **2011**, *5*, 914–922.
- [54] Dorn, M.; Lange, P.; Chekushin, A.; Severin, N.; Rabe, J. P. High contrast optical detection of single graphenes on optically transparent substrates. *J. Appl. Phys.* **2010**, *108*, 106101.
- [55] Gorbachev, R. V.; Riaz, I.; Nair, R. R.; Jalil, R.; Britnell, L.; Belle, B. D.; Hill, E. W.; Novoselov, K. S.; Watanabe, K.; Taniguchi, T. et al., Hunting for monolayer boron nitride: Optical and raman signatures. *Small* **2011**, *7*, 465–468.
- [56] Westheim, G. Optimal magnification in visual microscopy. *J. Opt. Soc. Am.* **1972**, *62*, 1502–1504.
- [57] Teo, G. Q.; Wang, H. M.; Wu, Y. H.; Guo, Z. B.; Zhang, J.; Ni, Z. H.; Shen, Z. X. Visibility study of graphene multilayer structures. *J. Appl. Phys.* **2008**, *103*, 124302.
- [58] Zeng, H.; Zhi, C.; Zhang, Z.; Wei, X.; Wang, X.; Guo, W.; Bando, Y.; Golberg, D. “White graphenes”: Boron nitride nanoribbons via boron nitride nanotube unwrapping. *Nano Lett.* **2010**, *10*, 5049–5055.
- [59] Siwy, Z. S. Ion-current rectification in nanopores and nanotubes with broken symmetry. *Adv. Funct. Mater.* **2006**, *16*, 735–746.
- [60] Shaw, R. S.; Packard, N.; Schröter, M.; Swinney, H. L. Geometry-induced asymmetric diffusion. *Proc. Natl. Acad. Sci. USA* **2007**, *104*, 9580–9584.
- [61] Guo, W.; Cao, L. X.; Xia, J. C.; Nie, F. Q.; Ma, W.; Xue, J. M.; Song, Y. L.; Zhu, D. B.; Wang, Y. G.; Jiang, L. Energy harvesting with single-ion-selective nanopores: A concentration-gradient-driven nanofluidic power source. *Adv. Funct. Mater.* **2010**, *20*, 1339–1344.
- [62] Cao, L. X.; Guo, W.; Ma, W.; Wang, L.; Xia, F.; Wang, S. T.; Wang, Y. G.; Jiang, L.; Zhu, D. B. Towards understanding the nanofluidic reverse electro dialysis system: Well matched charge selectivity and ionic composition. *Energy Environ. Sci.* **2011**, *4*, 2259–2266.
- [63] Guo, W.; Xia, H. W.; Cao, L. X.; Xia, F.; Wang, S. T.; Zhang, G. Z.; Song, Y. L.; Wang, Y. G.; Jiang, L.; Zhu, D. B. Integrating ionic gate and rectifier within one solid-state nanopore via modification with dual-responsive copolymer brushes. *Adv. Funct. Mater.* **2010**, *20*, 3561–3567.
- [64] Guo, W.; Xia, H.; Xia, F.; Hou, X.; Cao, L.; Wang, L.; Xue, J.; Zhang, G.; Song, Y.; Zhu, D. et al. Current rectification in temperature-responsive single nanopores. *ChemPhysChem* **2010**, *11*, 859–864.
- [65] Zhang, W. M.; Wang, Y. G.; Li, J.; Xue, J. M.; Ji, H.; Ouyang, Q.; Xu, J.; Zhang, Y. Controllable shrinking and shaping of silicon nitride nanopores under electron irradiation. *Appl. Phys. Lett.* **2007**, *90*, 163102.
- [66] Bertolazzi, S.; Brivio, J.; Kis, A. Stretching and breaking of ultrathin MoS₂. *ACS Nano*, in press, DOI:10.1021/nm203879f.